Contents lists available at ScienceDirect

Nuclear Inst. and Methods in Physics Research, A

Nuclei charge measurement by the Alpha Magnetic Spectrometer silicon tracker

Y. Jia [a],[*], Q. Yan [a], V. Choutko [a], H. Liu [a],[1], A. Oliva [b]

[a] Massachusetts Institute of Technology(MIT), Cambridge, MA 02139, USA
[b] Istituto Nazionale di Fisica Nucleare (INFN) Sezione di Bologna, I-40126 Bologna, Italy

ARTICLE INFO

ABSTRACT

The Alpha Magnetic Spectrometer (AMS) is a high energy particle detector aboard the International Space Station. AMS precisely measures the fluxes of all cosmic-ray nuclei with charge from $Z = 1$ to $Z = 28$ and beyond. The AMS silicon tracker measures energy deposition of charged particles traversing over nine-layer silicon sensors, from $L1$ to $L9$. In this paper, the details of the AMS silicon tracker charge measurement method are presented. The obtained charge resolution of the AMS inner tracker ($L2$ to $L8$ combined) is 0.1 charge units for carbon, 0.15 charge units for silicon, and 0.3 charge units for iron nuclei.

1. Introduction

The Alpha Magnetic Spectrometer (AMS) is a precision particle physics experiment operating on the International Space Station (ISS) since May 19, 2011. To date, AMS has collected more than 150 billion cosmic rays, and it will operate through the lifetime of the ISS, 2028 or beyond. The physics goals of AMS are the searches for dark matter, antimatter, and measurements of the cosmic ray fluxes in the GV-TV rigidity region. Precise knowledge of the rigidity dependences of the fluxes provides important insights into the origin, acceleration, and propagation of cosmic rays in the Galaxy [1–3].

The schematic of the AMS detector [4] is shown in Fig. 1. The key elements are the permanent magnet [5], the silicon tracker [6], the four planes of time of flight TOF scintillation counters [7], a transition radiation detector TRD [8], a ring imaging Cerenkov detector RICH [9], an electromagnetic calorimeter ECAL [10], and an array of 16 anticoincidence counters [11]. The AMS coordinate system is concentric with the center of the magnet. The x axis is parallel to the main component of the magnetic field, and the z axis points vertically. The (y-z) plane is the bending plane. The AMS silicon tracker has nine layers. The first ($L1$) at the top of the detector, the second ($L2$) just above the magnet, six ($L3$ to $L8$) within the bore of the magnet, and the last ($L9$) just above ECAL. $L2$ to $L8$ constitute the inner tracker.

The silicon tracker, together with the magnet, measures the rigidity, and it also determines the charge magnitude of nuclei by independent energy deposition measurements on multiple layers. To achieve the best possible accuracy on the charge measurements, a method with dedicated treatments of the detector effects has been developed.

2. AMS silicon tracker

The AMS silicon tracker is composed of 2264 double-sided microstrip sensors (72×41 mm^2, 300 μm thick) embedded in 192 independent modules called ladders. On opposite sides of the silicon sensor, the x- and y-side strips are implanted along orthogonal directions with implantation (readout) pitches of 27.5 (110) μm and 104 (208) μm, respectively [6]. The obtained spatial resolution for $2 \leq Z \leq 26$ is 5–9 μm in the bending direction y [12].

The readout strips in the silicon sensor are coupled to 64-channel low-noise, high dynamic range readout VA chips [13], located on a standard printed circuit board (hybrid). For each ladder, 6 VA chips are used for the x side and 10 VA chips for the y side. The structure of a ladder and the main components of the readout hybrids are described in Ref. [14]. The analog signal output from the readout hybrids is amplified and digitized in the Tracker Data Reduction boards (TDR), which consists of 12-bit Analog to Digital Converters (ADC).

A charged particle passing through the silicon generates electron–holes pairs along its path by ionization. Positive and negative charge carriers drift in opposite directions in the sensor electric field inducing a signal on the implanted strip on the silicon substrate surface. Additionally, capacitive coupling among strips redistributes the signal to neighboring strips around the particle impact position [15]. Fig. 2 illustrates the typical signal response of the four largest amplitude strips (A_1, A_2, A_3, A_4). The strip with the largest amplitude (A_1) is called the seed strip, located closest to the impact position of the passing particle.

The induced signal on the x and y sides provide independent measurements of the particle energy deposition ($dE/dx \propto Z^2$). Fig. 3

---

* Corresponding author.
 E-mail address: yi.jia@cern.ch (Y. Jia).
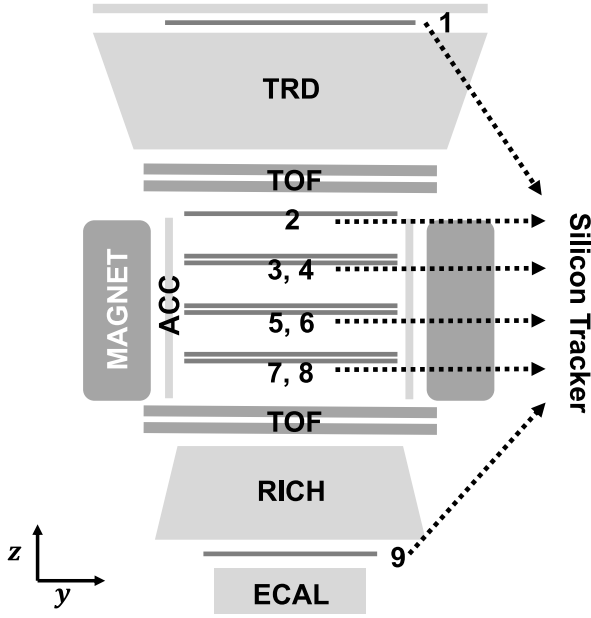[1] Now at Southwest Jiaotong University, Chengdu 611756, China.
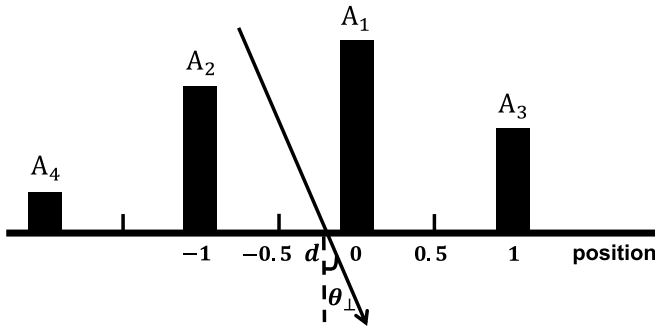
Fig. 1. Schematic of the AMS detector.

Fig. 2. The typical signal response of the four largest amplitude strips (A_1, A_2, A_3, A_4) in the silicon sensor. The seed strip (A_1) is located closest to the impact position of the passing particle. The second largest-amplitude strip (A_2), is next closest to the impact position. The third largest-amplitude strip (A_3) is located next to the seed strip on the other side. The fourth largest-amplitude strip (A_4) is located next to the second strip. The arrow indicates the impact position d and direction of the passing particle with an inclination angle $\theta_\perp$ in the plane perpendicular to the direction of the strips.

Fig. 3. The signal responses $\sqrt{A_i}$ ($i = 1, 2, 3$) in units of ADC counts as functions of nuclei charge Z at a given position $d \sim 0.3$ and inclination angle $\theta_\perp \sim 10°$ for (a) the x side and (b) the y side.

Fig. 4. The $\sqrt{A_1}$ distributions (histograms) and the fits (dashed lines) from two VAs on the y side for an oxygen nuclei sample.

shows the signal responses of three strips with the largest amplitudes (A_1, A_2, A_3) as functions of the nuclei charge Z at a given position and inclination angle $\theta_\perp$. For the x side as shown in Fig. 3(a), A_1 has a linear response in the region $1 \leq Z \leq 8$ and gradually saturates in the region $Z \geq 10$ due to ADC limitation; A_2 response is first linear and starts to saturate in the region $Z \geq 16$; A_3 response does not saturate in the entire charge range. To accommodate measurement up to the highest possible charge, electronics in the y side is designed to have a different response. As seen in Fig. 3(b), A_1 response is linear for $1 \leq Z \leq 3$, followed by a nonlinear region for $4 \leq Z \leq 9$ and again a linear region for $10 \leq Z \leq 20$, then it gradually saturates for $Z \geq 20$; A_2 response is nonlinear for $6 \leq Z \leq 16$ and linear in the regions $1 \leq Z \leq 5$ and $Z \geq 17$; A_3 signal amplitude steadily increases in the entire charge range.

To achieve the best accuracy on the tracker charge, the nuclei charge measurement is built by combining the signal of all individual strips ($A_1, A_2, A_3, \ldots$).
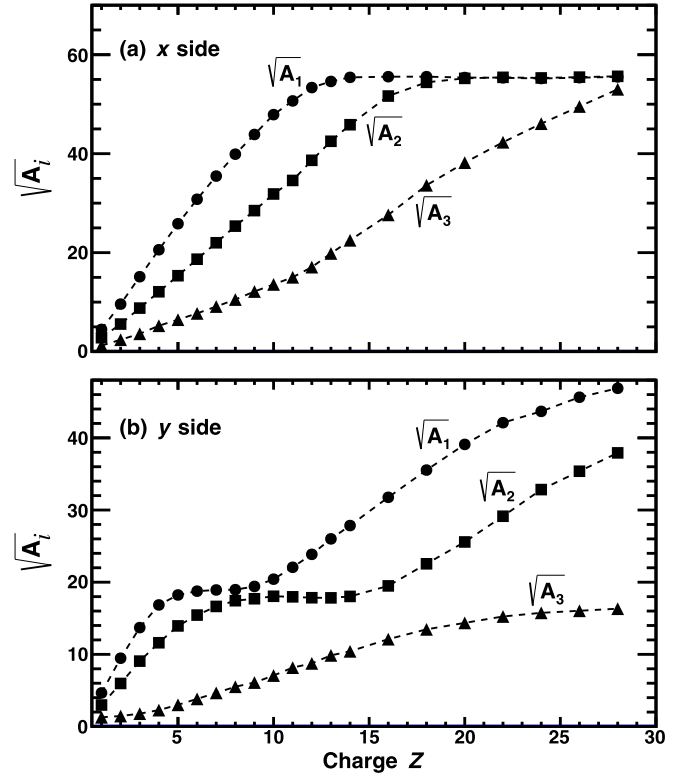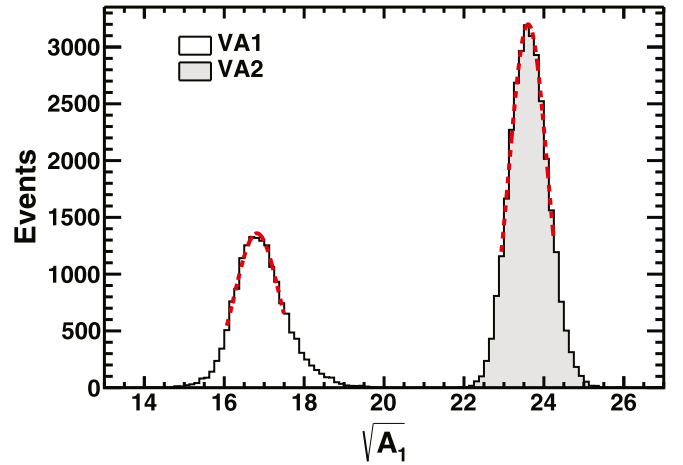
3. Tracker charge measurement

The tracker charge measurement has to take account of several effects regarding the responses of readout elements, particle impact position and angular dependence, velocity dependence of the energy loss, and time variation of the gain. The corresponding correction for each effect is applied subsequently to optimize the charge measurement. In-flight calibration of the tracker charge measurement is performed by using the first seven years of the AMS data. The sample for each nuclei species from proton to nickel used in the calibration is selected by charge measured by the TOF.
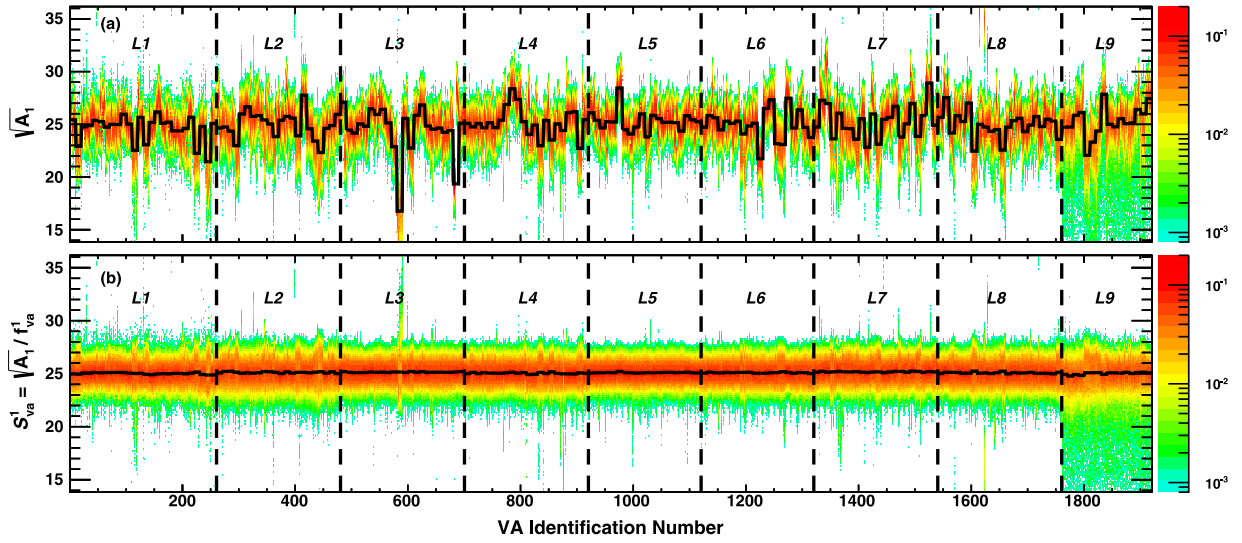
Fig. 5. The signal distribution for silicon (a) before and (b) after the equalization for the *y*-side seed strips from 1920 VA chips labeled by the VA identification number. The values of color code on the right indicate the density probability of the events for each VA. The horizontal solid lines represent the average signal values of 10 VAs in one ladder. These lines are connected to guide the eye. VAs in different layers are separated by dashed lines. (For interpretation of the references to color in this figure legend, the reader is referred to the web version of this article.)
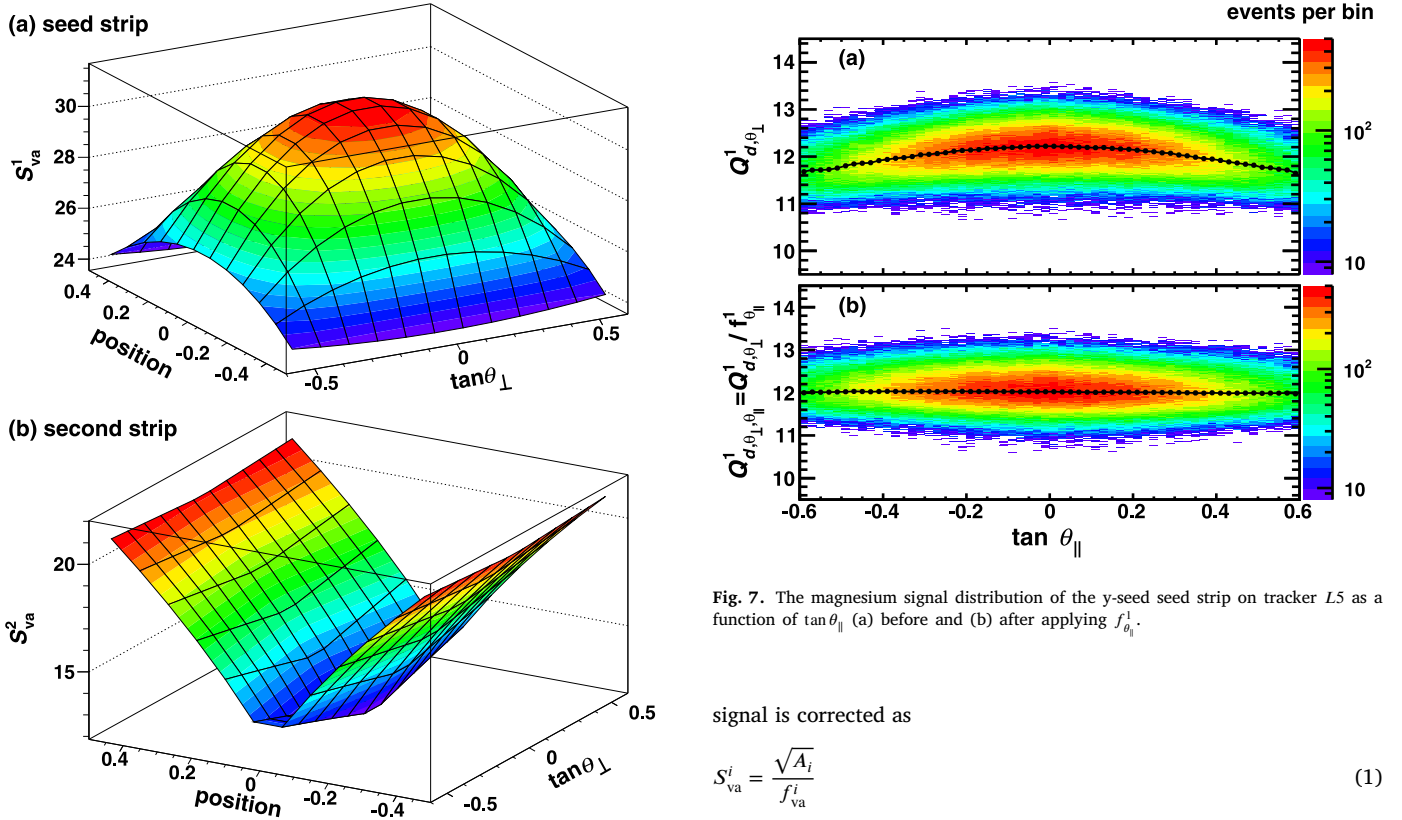

Fig. 6. Position and $\tan\theta_{\perp}$ dependence of the *y*-side signal with a silicon nuclei sample for the (a) seed strip and (b) second strip.

3.1. Readout element equalization

Each VA chip exhibits different response. For each nuclei species, the strip amplitude distribution on each VA chip is fitted to extract its Most Probable Value (MPV). As an example, Fig. 4 shows the $\sqrt{A_1}$ distributions from two VAs for an oxygen nuclei sample. The measured

Fig. 7. The magnesium signal distribution of the y-seed seed strip on tracker *L5* as a function of $\tan\theta_{\parallel}$ (a) before and (b) after applying $f_{\theta_{\parallel}}^1$.

signal is corrected as

$$S_{va}^i = \frac{\sqrt{A_i}}{f_{va}^i} \tag{1}$$

where $\sqrt{A_i}$ and S_{va}^i are the signal of *i*th ($i = 1, 2, 3, \ldots$) strip before and after the VA equalization respectively, and f_{va}^i is the equalization factor used to equalize the response for each individual VA.

MPV is extracted for each nuclei species from proton to nickel, and for each VA, thus a total of 3072 VA chips (1152 on the *x* side and 1920 on the *y* side) are calibrated. Such a procedure is applied on each individual strip ($A_1, A_2, A_3, \ldots$). To minimize the effect of energy loss velocity dependence discussed in Section 3.3, the calibration sample is required to have the measured rigidity larger than 7 GV.

As an example, Fig. 5 shows the signal distribution for silicon before and after the equalization for the *y*-side seed strips from 1920 VA chips.
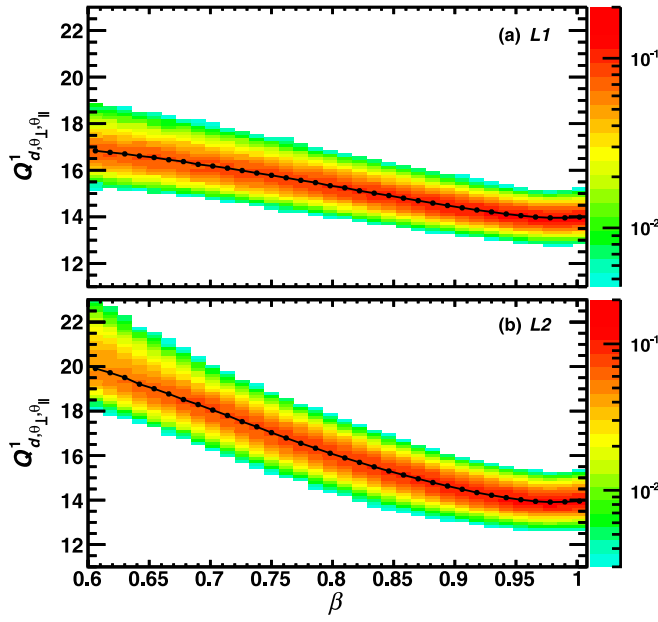
Fig. 8. The silicon signal distribution of the y-side seed strip on tracker (a) $L1$ and (b) $L2$ as a function of the β. The color code on the right indicates the density probability of the events for each β bin. The difference between $L1$ and $L2$ is due to the particle energy losses in materials. (For interpretation of the references to color in this figure legend, the reader is referred to the web version of this article.)
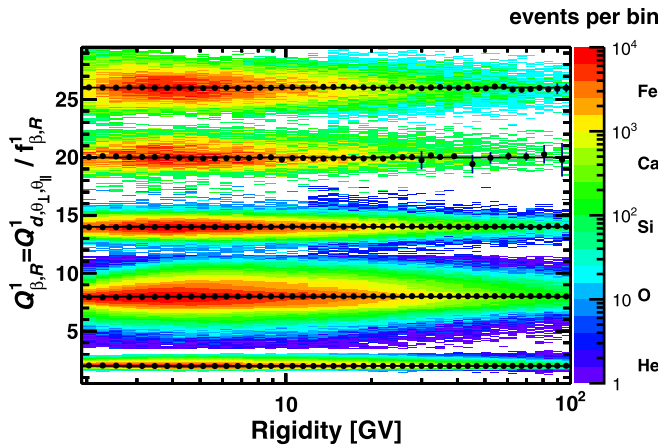

Fig. 9. The charge distribution of the y-side seed strip on tracker $L2$ as functions of rigidity for He, O, Si, Ca, and Fe nuclei after correction. Lines are fits of constant values.

As seen, the response of different detector readout elements becomes homogeneous after this correction.

3.2. Position and angular corrections

For a given strip, the deposited signal exhibits large dependences on the particle impact position d and the inclination angles $\theta_\perp$ and $\theta_\parallel$ (measured in the plane parallel to the strips) of the particle. As an example, Fig. 6 shows the position and $\tan\theta_\perp$ dependence of the y-side signal with a silicon nuclei sample for the seed strip and second strip. For the seed strip, the maximum signal collection appears at the center of the plot where the particle impacts vertically on the seed strip. For the second strip, the maximums are located at the edge of the plot where the particle passes through the middle between the seed and the second strips.

Similar to the previous procedure, the signal distribution on each position d and $\tan\theta_\perp$ is fitted to extract the corresponding MPV value

(MPV$_{d,\theta_\perp}$). With these MPV values, the position and $\tan\theta_\perp$ correction map is built for each nuclei sample from proton to nickel and the measured rigidity is required to be larger than 7 GV. The signal is corrected as

$$Q^i_{d,\theta_\perp} = \frac{S^i_{va}}{f^i_{d,\theta_\perp}}. \tag{2}$$

where $Q^i_{d,\theta_\perp}$ is the strip signal after the position and $\theta_\perp$ correction, and $f^i_{d,\theta_\perp} = \text{MPV}_{d,\theta_\perp}/Z$ is the correction factor where Z is the integer charge determined by the TOF.

After correcting d and $\theta_\perp$, the MPV values are extracted again for different $\theta_\parallel$ to account for the path length of the particle in the silicon sensor. Finally, the charge after the position and angular correction $Q^i_{d,\theta_\perp,\theta_\parallel}$ is given by

$$Q^i_{d,\theta_\perp,\theta_\parallel} = \frac{Q^i_{d,\theta_\perp}}{f^i_{\theta_\parallel}}. \tag{3}$$

As an example, Fig. 7 shows the magnesium signal distribution of the y-side seed strip on tracker $L5$ as a function of $\tan\theta_\parallel$ before and after applying $f^1_{\theta_\parallel}$.

3.3. Velocity and rigidity corrections

The energy loss of the particle depends on its velocity β as described by the Bethe–Bloch formula [16]. This can be seen in Fig. 8 which shows the silicon signal distribution of the y-side seed strip on tracker $L1$ and $L2$ as a function of the measured velocity β.

To obtain an energy-independent charge measurement, the velocity β measured by the TOF and the rigidity R measured by the silicon tracker are used for the correction. First, the signal distributions for different β regions are fitted to extract their MPV values. After that, the MPV values are extracted again for different R to further reduce the residual energy dependence. The measured charge by each individual strip after the velocity and rigidity corrections $Q^i_{\beta,R}$ is given by

$$Q^i_{\beta,R} = \frac{Q^i_{d,\theta_\perp,\theta_\parallel}}{f^i_{\beta,R}}. \tag{4}$$

After the corrections, the charge distribution of the y-side seed strip on tracker $L2$ as functions of rigidity for He, O, Si, Ca, and Fe nuclei is shown in Fig. 9.

3.4. Time dependent correction

The thermal environment of AMS is constantly changing due to variations of the solar beta angle [17], the position of the ISS solar arrays [18], etc. Even though the tracker temperature is being continuously monitored and controlled [19,20], the existing variation can introduce a small change in the tracker gain and degrade the charge performance.

After previous calibration steps, the daily time variation of single-strip charge measurements is estimated to be < 2% for all nuclei samples. The variation within one day is negligible. The corrected charge sample is further divided into one-day time intervals. The charge distribution for each interval is fitted to extract its MPV value for each nuclei species from proton to nickel. To maximize the statistics, we accumulate the event sample from all readout elements of each tracker layer in the full energy range. The measured charge is corrected as

$$Q^i = \frac{Q^i_{\beta,R}}{f^i_t}. \tag{5}$$

where Q^i is the charge after the time dependent correction. The correction f^i_t is extracted from MPV value of each individual strip.

Fig. 10 shows the silicon charge distribution of the y-side seed strip on tracker $L2$ as a function of time before and after the time dependent correction. As seen, the measured charge is stable as a function of time after the correction.
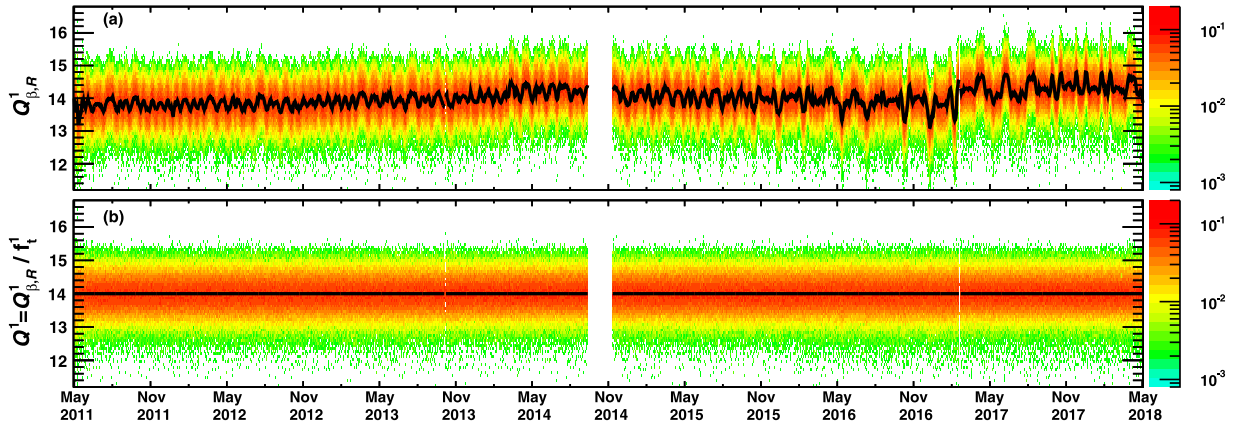
Fig. 10. The silicon charge distribution of the y-side seed strip on tracker $L2$ as a function of time (a) before and (b) after the time dependent correction. Each time bin is one day. The average charge values for each day are connected by lines to guide the eye. Color code on the right indicates the density probability of the events in one day. The data near November 2014 are not presented as AMS was performing detector studies over this period. (For interpretation of the references to color in this figure legend, the reader is referred to the web version of this article.)
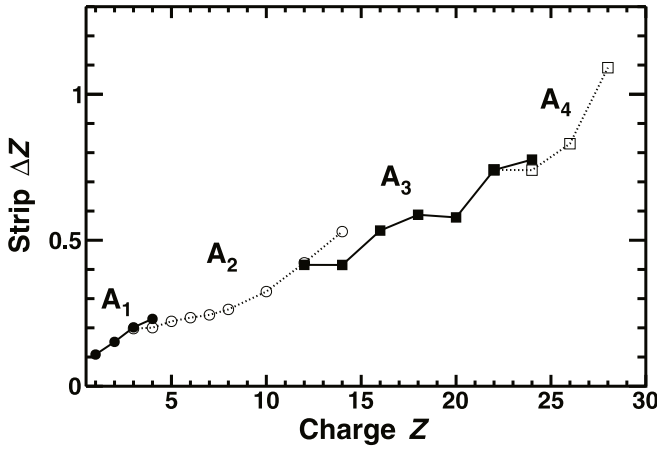

Fig. 11. The x-side charge resolution ΔZ as a function of nuclei charge Z for individual strips A_1 (solid circles), A_2 (open circles), A_3 (solid squares), and A_4 (open squares).

Fig. 12. The charge distribution on tracker $L2$ for $1 \leq Z \leq 8$ selected by the TOF, tracker $L1$, and tracker $L3$-$L8$ with rigidity > 7 GV. The peak value of each species is normalized to 1.

4. Tracker charge measurement performance

After repeating all the calibration procedures to each individual strip, the final charge measurement is made with the combination of all measured strips from either a single layer or several layers combined. In this section, the method to obtain the combined charge is described, and the performance of the tracker charge measurement is presented.

4.1. Single layer charge and inner tracker charge

First, the measurements from individual strips, as shown in Fig. 11 for x side, are combined to each single layer measurement on x side and y side respectively by

$$Q_{lx} = \frac{\sum_{i=1} Q_x^i \cdot w_x^i}{\sum_{i=1} w_x^i}, \quad Q_{ly} = \frac{\sum_{i=1} Q_y^i \cdot w_y^i}{\sum_{i=1} w_y^i} \tag{6}$$

where Q_{lx} and Q_{ly} are the combined charge for x side and y side on a single layer, $w_x^i = 1/(\Delta \tilde{Q}_x^i)^2$ and $w_y^i = 1/(\Delta \tilde{Q}_y^i)^2$ are the weights calculated from the measured charge resolutions $\Delta \tilde{Q}_x^i$ and $\Delta \tilde{Q}_y^i$ respectively. In the first iteration, the charge resolution of each individual strip $\Delta \tilde{Q}_x^i$ or $\Delta \tilde{Q}_y^i$ is evaluated from its own measurement as $\Delta \tilde{Q}_x^i = \Delta Q_x^i$ or $\Delta \tilde{Q}_y^i = \Delta Q_y^i$. In the next a few iterations, $\Delta \tilde{Q}_x^i$ or $\Delta \tilde{Q}_y^i$ is more accurately evaluated from the layer charge as $\Delta \tilde{Q}_x^i = \Delta Q_{lx}$ or $\Delta \tilde{Q}_y^i = \Delta Q_{ly}$.
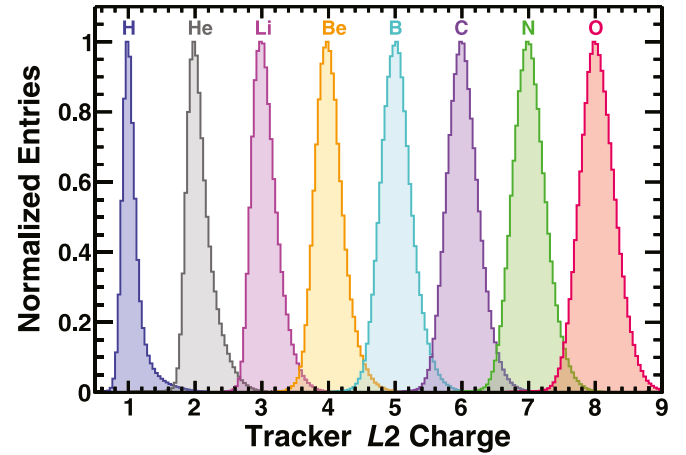
The single layer charge Q_l is calculated as a weighted sum of the x- and y-side charge measurements:

$$Q_l = \frac{Q_{lx} w_{lx} + Q_{ly} w_{ly}}{w_{lx} + w_{ly}} \tag{7}$$

where $w_{lx} = 1/(\Delta \tilde{Q}_{lx})^2$ and $w_{ly} = 1/(\Delta \tilde{Q}_{ly})^2$ are the weights determined in a few iterations similarly as before. As an example, Fig. 12 shows the charge distribution on tracker $L2$ for $1 \leq Z \leq 8$.

The measurements from tracker $L2$ to $L8$ are combined to the inner tracker charge values Q_x and Q_y for the x and y side respectively by

$$Q_x = \frac{1}{n_x} \sum_l Q_{lx}, \quad Q_y = \frac{1}{n_y} \sum_l Q_{ly} \tag{8}$$

where Q_{lx} or Q_{ly} is the charge measurement from layer l, n_x or n_y is the number of layers with measurements. In this calculation, measurements with large deviations compared to the average measurement or those layers with dead strip nearby the measured strips are excluded.

After the combination, the inner tracker measured charge derived from x or y side is obtained. Fig. 13 shows the correlation between the x-side inner tracker charge Q_x and the y-side inner tracker charge Q_y.

Finally, the inner tracker charge Q is calculated as a weighted sum of the x and y side charge measurements:
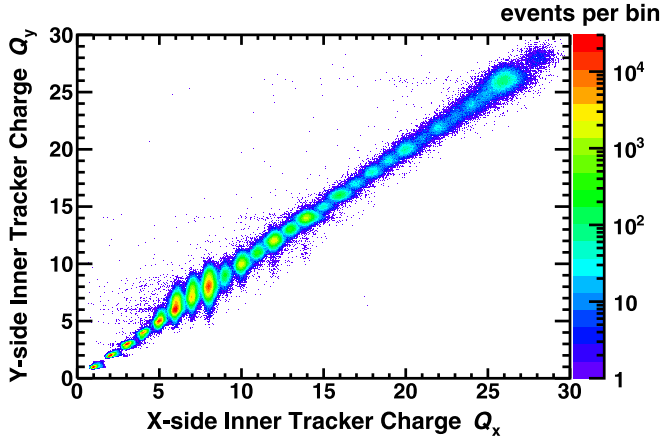
$$Q = \frac{Q_x w_x + Q_y w_y}{w_x + w_y} \tag{9}$$

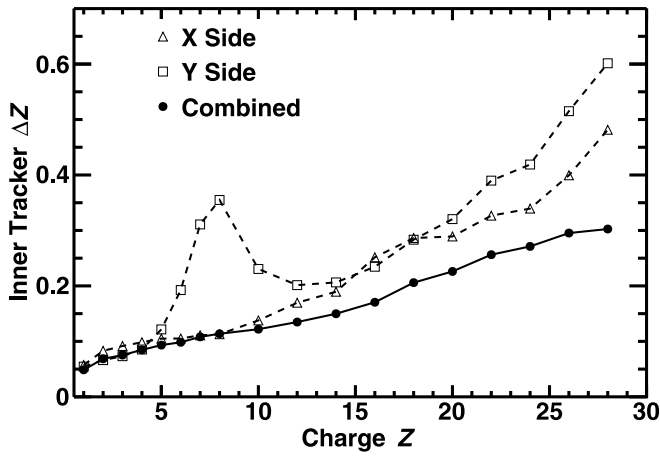Fig. 13. Correlation between the x-side inner tracker charge Q_x and the y-side inner tracker charge Q_y.

Fig. 14. The charge resolution ΔZ in charge units for x-side (open triangles), y-side (open squares) and combined (solid circles) inner tracker charge as functions of nuclei charge Z with rigidity > 7 GV.
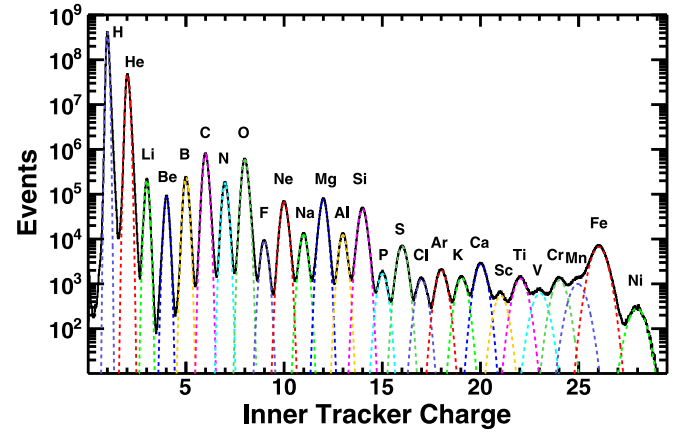

Fig. 15. The inner tracker charge distribution for the measured cosmic ray nuclei with rigidity > 7 GV. Dashed lines are Gaussian fits for each nuclear charge. The charge identification is done solely by the inner tracker.
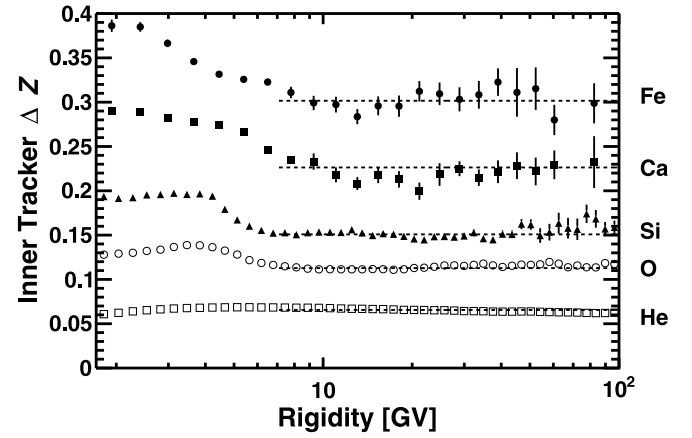

Fig. 16. The inner tracker charge resolution ΔZ as functions of rigidity for He, O, Si, Ca, and Fe nuclei. Dashed lines are fits of constant values above 7 GV.

Table 1
The charge resolutions ΔZ in charge units (c.u.) of the AMS inner tracker for elements with $1 \leq Z \leq 8$, and event Z for $10 \leq Z \leq 28$.

Charge Z	1	2	3	4	5	6	7	8	10
Element	H	He	Li	Be	B	C	N	O	Ne
ΔZ (c.u.)	0.05	0.07	0.08	0.08	0.09	0.10	0.11	0.11	0.12
Charge Z	12	14	16	18	20	22	24	26	28
Element	Mg	Si	S	Ar	Ca	Ti	Cr	Fe	Ni
ΔZ (c.u.)	0.13	0.15	0.17	0.21	0.23	0.26	0.27	0.30	0.30

where $w_x = 1/(\Delta \tilde{Q}_x)^2$ and $w_y = 1/(\Delta \tilde{Q}_y)^2$ are the weights determined in a few iterations similarly as before. Fig. 14 shows the obtained charge resolution comparison of the x-side, y-side and combined for $1 \leq Z \leq 28$. As seen, the performance of the combined charge is better than any single-side measurement from either x or y side.

Fig. 15 shows the combined inner tracker charge distribution for the measured cosmic ray nuclei. As seen, different cosmic-ray nuclei species are well separated.

4.2. Charge resolution

The performance of charge measurement at low rigidities below 7 GV is affected by energy loss velocity dependence, as shown in Fig. 16 for the charge resolution of the inner tracker charge as functions of rigidity for He, O, Si, Ca, and Fe nuclei. At high rigidities above 7 GV, the tracker charge is rigidity-independent for all nuclei.

In the region $R > 7$ GV, charge resolutions are obtained for nuclei species with $1 \leq Z \leq 28$ as summarized in Table 1. Fig. 17(a) shows the charge resolution ΔZ of the inner tracker ($L2$-$L8$) and a single layer as functions of nuclei charge Z. As seen, the resulting charge resolution increases steadily as functions of charge Z. The measured resolution of the inner tracker charge is 0.1 charge units for carbon, 0.15 charge units for silicon, and 0.3 charge units for iron. For a single layer, ΔZ is 0.2 charge units for carbon, 0.4 charge units for silicon, and 0.8 charge

units for iron. Fig. 17(b) shows the $\Delta Z/Z$ of the inner tracker and a single layer. As seen, $\Delta Z/Z$ is approaching a constant value ~ 0.01 in the region $Z \geq 14$.

5. Conclusions

A complete procedure of the AMS silicon tracker charge measurement has been discussed, including detector effects, such as VA gain, particle impact position and inclination angle dependence, velocity dependence of the energy loss, and the time variation of the gain. The procedure allows a precise charge determination for every single tracker strip, that further combines into a charge for a single layer, and for the entire inner tracker.

The obtained AMS inner tracker charge resolution is 0.1 charge units for carbon, 0.15 charge units for silicon, and 0.3 charge units
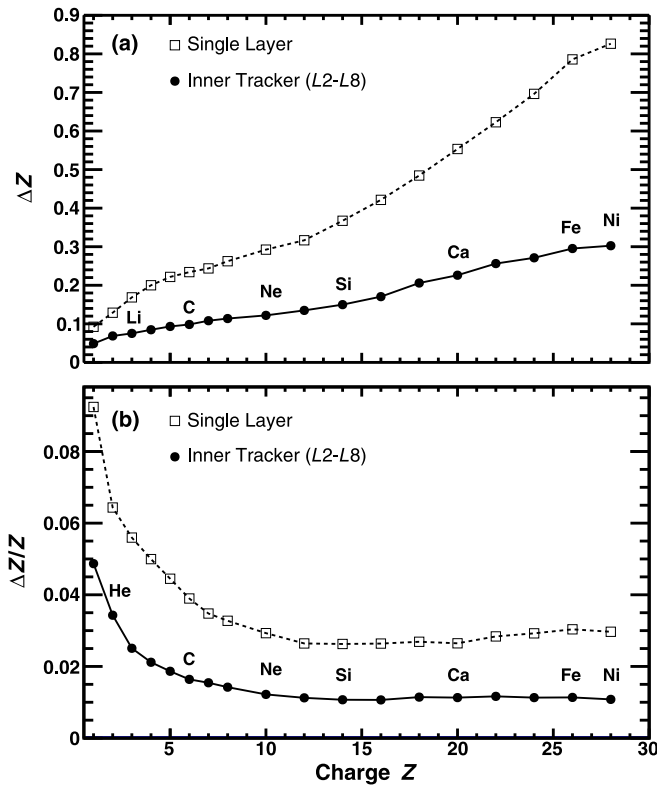
Fig. 17. (a) Charge resolution ΔZ and (b) $\Delta Z/Z$ of the inner tracker (circles) and a single layer (squares) as functions of nuclei charge Z with rigidity > 7 GV. As seen in (b), $\Delta Z/Z$ is approaching a constant value ~0.01 for high Z.

for iron. The achieved accuracy of the tracker charge allows AMS to precisely measure the cosmic ray fluxes in the charge region $1 \leq Z \leq 28$ and beyond.

Declaration of competing interest

The authors declare that they have no known competing financial interests or personal relationships that could have appeared to influence the work reported in this paper.

References

[1] I.A. Grenier, J.H. Black, A.W. Strong, The nine lives of cosmic rays in galaxies, Annu. Rev. Astron. Astrophys. 53 (2015) 199–246.

[2] P. Blasi, The origin of galactic cosmic rays, Astron. Astrophys. Rev. 21 (2013) 70.

[3] A.W. Strong, I.V. Moskalenko, V.S. Ptuskin, Cosmic-ray propagation and interactions in the galaxy, Annu. Rev. Nucl. Part Sci. 57 (2007) 285–327.

[4] A. Kounine, The alpha magnetic spectrometer on the international space station, Int. J. Mod. Phys. E 21 (2012) 1230005.

[5] K. Lübelsmeyer, et al., Upgrade of the alpha magnetic spectrometer (AMS-02) for long term operation on the international space station (ISS), Nucl. Instrum. Methods Phys. Res. A 654 (2011) 639–648.

[6] B. Alpat, et al., The internal alignment and position resolution of the AMS-02 silicon tracker determined with cosmic-ray muons, Nucl. Instrum. Methods Phys. Res. A 613 (2010) 207–217.

[7] V. Bindi, et al., Calibration and performance of the AMS-02 time of flight detector in space, Nucl. Instrum. Methods Phys. Res. A 743 (2014) 22–29.

[8] T. Kirn, et al., The AMS-02 TRD on the international space station, Nucl. Instrum. Methods Phys. Res. A 706 (2007) 43–47.

[9] M. Aguilar, et al., In-beam aerogel light yield characterization for the AMS RICH detector, Nucl. Instrum. Methods Phys. Res. A 614 (2010) 237–249.

[10] C. Adloff, et al., The AMS-02 lead-scintillating fibres Electromagnetic Calorimeter, Nucl. Instrum. Methods Phys. Res. A 714 (2013) 147–154.

[11] P. von Doetinchem, et al., The AMS-02 anticoincidence counter, Nucl. Phys. B 197 (2009) 15–18.

[12] G. Ambrosi, V. Choutko, C. Delgado, A. Oliva, Q. Yan, Y. Li, The spatial resolution of the silicon tracker of the Alpha Magnetic Spectrometer, Nucl. Instrum. Methods Phys. Res. A 869 (2017) 29–37.

[13] O. Toker, et al., VIKING, a CMOS low noise monolithic 128 channel front end for Si-strip detector readout, Nucl. Instrum. Methods Phys. Res. A 340 (1994) 572–579.

[14] J. Alcaraz, et al., The alpha magnetic spectrometer silicon tracker: Performance results with protons and helium nuclei, Nucl. Instrum. Methods Phys. Res. A 593 (2008) 376–398.

[15] E. Belau, et al., Charge collection in silicon strip detectors, Nucl. Instrum. Methods Phys. Res. 214 (1983) 253–260.

[16] M. Tanabashi, et al., Review of particle physics, Phys. Rev. D 98 (2018) 030001.

[17] K. Wang, et al., Operations of the thermal control system for Alpha Magnetic Spectrometer electronics following the beta angle of the International Space Station, Nucl. Instrum. Methods Phys. Res. A 767 (2014) 235–244.

[18] C. Zheng, et al., Investigations on the thermal condition of the Alpha Magnetic Spectrometer on the International Space Station during the maneuver of locking solar arrays, Nucl. Instrum. Methods Phys. Res. A 910 (2018) 96–105.

[19] G. Alberti, et al., Active CO_2 two-phase loops for the AMS-02 tracker, IEEE Aerosp. Electron. Syst. Mag. 29 (2014) 4–13.

[20] Y. Yu, et al., Design and application of thermal mass flow meter in space, Nucl. Instrum. Methods Phys. Res. A 950 (2020) 163003.